Development and Control of a Low-Cost Linear Variable-Reluctance Motor for Precision Manufacturing Automation

Wai-Chuen Gan, *Member, IEEE,* and Norbert C. Cheung

***Abstract*—Most advanced manufacturing processes require precise linear-position control for material transfer, packaging, assembly, and electrical wiring. To achieve precise linear motion, most of these high-performance manufacturing machines use *X–Y* sliding tables with permanent-magnet rotary motors and rotary-to-linear couplers. Though this method is the most widely used, it has disadvantages of low accuracy, complex mechanical adjustments, high cost, and low reliability. This paper describes the use of the variable-reluctance-driving principle to construct a novel linear direct-drive actuator system for high-performance position control in manufacturing automation. The proposed actuator has a very simple structure and it can be manufactured easily. There is no need for magnets and no limitation on the traveling distance. The actuator is extremely robust and can be used in hostile environment. A novel control method, using cascade control and the force-linearization technique, is developed and implemented for precision position control of the actuator. Experimental results of the motion system indicate that the system has fast responses with good accuracy.**

***Index Terms*—Linear variable-reluctance motor (LVRM), lookup table force linearization, low-cost implementation, precision manufacturing automation.**

I. Introduction

VARIABLE reluctance motors (VRMs) have never been a popular choice for high-precision and high-speed motion actuators because it is difficult to control and its output has high torque ripples. This is due to the fact that the actuator's characteristic is highly dependent on its complex magnetic circuit, which is difficult to model, simulate, and control. There is little in recent literature which concerns high-performance motion control of variable-reluctance linear drive systems. It was only in recent years when we saw a general surge of interest in the VRM [1]–[4]. This was mostly due to the advancement of power electronics, digital signal processing, and the advance control algorithms for nonlinear systems. The present literature on linear VRM (LVRM) development seldom targets high-precision position control applications, such as semiconductor bonding machines and pick-and-place machines. In [5] and [7], the development of an LVRM is discussed but the application of this LVRM is mainly for transportation systems, and the control output is velocity. In [8] and [9], a detailed motor-design procedure and a motor-control algorithm are given, but the control output is again velocity control. In [10] and [11], the development of two LVRMs using the double-sided configuration is addressed; however, this motor configuration is not suitable for applications that have mechanical moving parts installed on one of the motor surfaces.

The purpose of the project is to develop a novel, high-performance, direct-drive, and linear motion actuator system for precision position control applications. The actuator is based on variable-reluctance technology [1], [4]. The linear direct-drive actuator has a simple and robust structure with low inertia and direct-drive capability, and is particularly suitable for high-precision and high-speed manufacturing machinery. Manufacturing of the actuator is simple, and it is suitable for precision travel over long distances. Unlike other types of motion actuators, mechanical couplings, lead screws, magnets, and brushes are not required in variable-reluctance linear actuators [14]. Neither are special mechanical adjustments or alignments necessary. Compared with permanent-magnet linear motors, the proposed actuator has a much simpler structure and is less expensive. It is also more robust and more fault tolerant, and has less of an overheating problem.

The organization of this paper is as follows. The construction of the motion actuator is discussed in Section II and the modeling of the LVRM is presented in Section III. The lookup table force-linearization scheme and the overall control strategy of the motor drive are introduced in Section IV. In Section V, the detailed hardware implementation of the proposed motion system is discussed. Experimental results on both long- and short-distance travels are reported in Section VI. Finally, concluding remarks are given in Section VII.

II. Construction of Motion Actuator

Fig. 1 shows the design schematic of the linear variable-reluctance motion system and Fig. 2 shows the actual model. The actuator is optimized for: 1) high power-to-size ratio; 2) low force ripple; 3) low leakage and eddy current loss; 4) fast current dynamics. The linear actuator design is based on VRM technology with longitudinal configuration [6]. Three-phase coil windings with 120 electrical degree separation are employed in the variable-reluctance actuator. Fig. 3 shows the three-phase coil arrangement with flux decoupling path. The novel feature of flux decoupling leads to a simpler motor model and a more robust motor structure [5], [6]. The tracking guide and the core of the

Manuscript received February 28, 2001; revised December 12, 2002. This work was supporte by the Hong Kong Research Grants Council under the Competitive Earmarked Research Grant PolyU5100/99E.

W.-C. Gan was with the Department of Electrical and Electronic Engineering, The Hong Kong University of Science and Technology, Hong Kong. He is now with ASM Assembly Automation Ltd., Hong Kong.

N. C. Cheung is with the Department of Electrical Engineering, The Hong Kong Polytechnic University, Hong Kong (e-mail: eencheun@polyu.edu.hk).

Digital Object Identifier 10.1109/TMECH.2003.816827

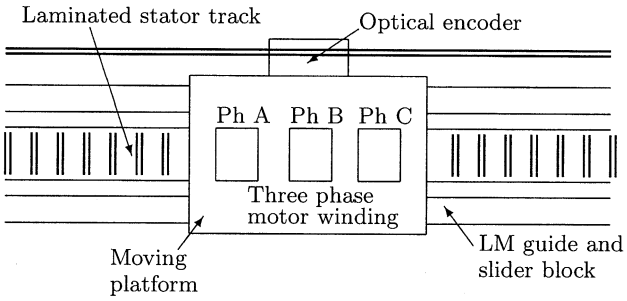

Fig. 1. Schematic of the linear VRM.

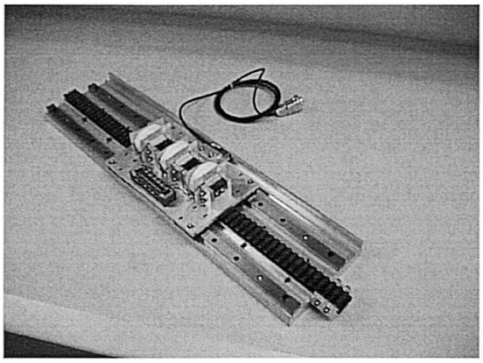

Fig. 2. Photo of the prototype motor.

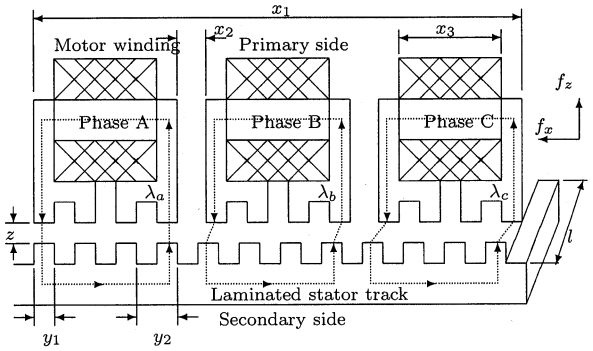

Fig. 3. Three-phase flux decoupled motor windings.

windings are laminated with 0.5-mm silicon steel plates. The motor is integrated on a precision linear motion guide. A linear optical encoder is mounted on the motion actuator to observe the motion profile and to provide the position feedback. Table I summarizes the characteristics of the proposed LVRM.

III. Modeling of Linear Variable Reluctance Motion Actuator

The nonlinear model of the proposed LVRM is discussed in this section. The nonlinear model of the LVRM is given by

$$f_x\left(i_a(t), i_b(t), i_c(t), x(t)\right) = \sum_{j=a}^{c} f_j\left(i_j(t), x(t)\right) = M_m \frac{d^2x(t)}{dt^2} + B_m \frac{dx(t)}{dt} + f_l(t) \quad (1)$$

TABLE I
Linear Variable-Reluctance Motor Characteristic

Power output	100W
Traveling distance	300mm
Maximum load	5kg
Position accuracy	$\pm 25\mu$m
Pole width	5mm (y_1)
Pole pitch	10mm (y_2)
Coil separation	8.333mm (x_2)
Winding width	15mm (x_3)
Air gap width	0.4mm (z)
Feedback device	Optical encoder with 1μm accuracy

and

$$f_j\left(i_j(t), x(t)\right) = \frac{\partial \int_0^{i_j} \lambda_j\left(i_j(t), x(t)\right) di_j}{\partial x(t)} \quad (2)$$

$$v_j(t) = R_j i_j(t) + \frac{\partial \lambda_j\left(i_j(t), x(t)\right)}{\partial x(t)} \frac{dx(t)}{dt} + \frac{\partial \lambda_j\left(x(t), i_j(t)\right)}{\partial i_j(t)} \frac{di_j(t)}{dt} \quad (3)$$

where $v_j(t)$, $i_j(t)$, R_j, and $\lambda_j(i_j(t), x(t))$ are the phase voltage, phase current, phase resistance, and phase flux linkage respectively, $x(t)$ is the travel distance, $f_x(i_a(t), i_b(t), i_c(t), x(t))$ is the generated electromechanical force, $f_l(t)$ is the external load force, and M_m and B_m are the mass and the friction constant, respectively.

This mathematical model consists of two parts. The first part is the linear model for the mechanical linkage while the second part is the nonlinear force-generation function. The mechanical parameters M_m and B_m can easily be found using standard experiments. The total nonlinear force-generation function $f_x(i_a(t), i_b(t), i_c(t), x(t))$ has three components: $f_a(i_a(t), x(t))$, $f_b(i_b(t), x(t))$, and $f_c(i_c(t), x(t))$. As these three functions are identical, the modeling of the total force-generation function can be derived from the modeling of the force-generation function for one phase $f_j(i_j(t), x(t))$. Therefore, a three-dimensional (3-D) force-current-position graph of the phase A winding can be measured experimentally to capture both the linear and saturation regions of the proposed LVRM.

A special test rig, as shown in Fig. 4, is designed and manufactured for the measurement of the force-current-position 3-D chart. This test rig is not only designed for this particular LVRM design, but can also be used for the measurement of other LVRMs without any modifications. This test rig can accurately divide the 5-mm pole width into 60 divisions using high-precision screws and gears. In the experiment, the test rig is used to lock the moving platform at 61 discrete positions (60 divisions) within a pole width (5 mm). After fixing the mechanical position, the computer can control the power switch, measure the force values automatically at 61 discrete phase current values (from 0 to 10 A) and finally construct the data base of the 3-D force-current-position chart. The choice of the 61 discrete positions is to ensure that an accurate measurement

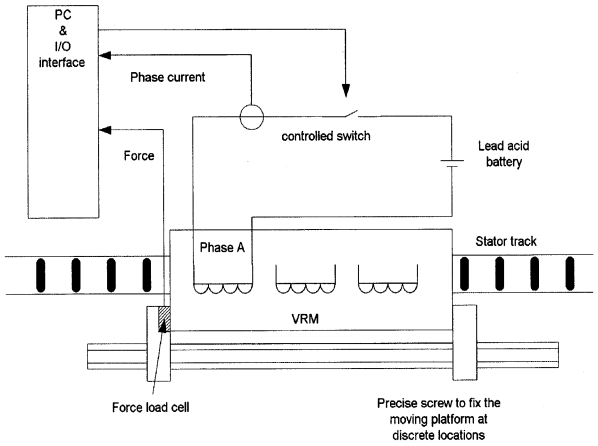

Fig. 4. Test rig for the force-current-position 3-D chart measurement.

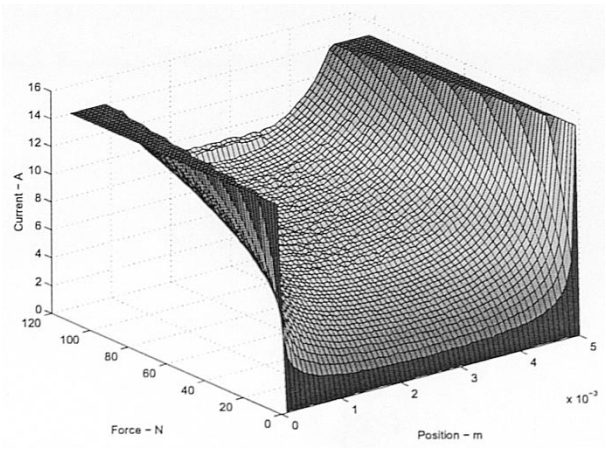

Fig. 6. Experimental current-force-position 3-D chart.

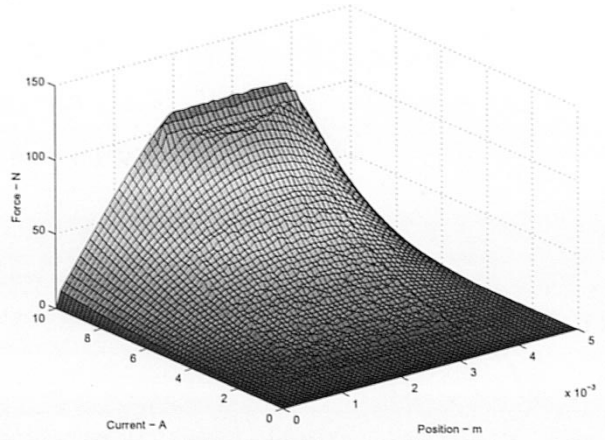

Fig. 5. Experimental force-current-position 3-D chart.

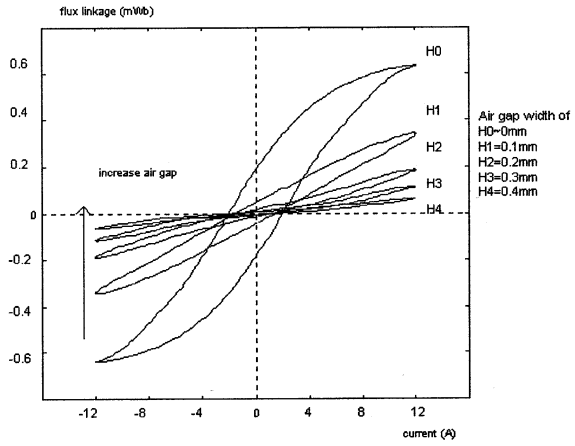

Fig. 7. Variation of hysteresis loop with airgap distance.

can be done using the mechanical test rig. The experimental force-current-position 3-D chart is shown in Fig. 5.

The second experiment is done to find out the relationship of the current-force-position needed for the force-linearization scheme in the real-time controller implementation that will be introduced in next section. The experiment is conducted by fixing the moving platform at 61 discrete positions within a pole width (5 mm). Then, the current required to generate the force at 61 discrete values from 0 to 110 N is measured. The experimental data are shown in Fig. 6. Both the data bases of the 3-D force-current-position and current-force-position are converted into MATLAB/SIMULINK models for the simulation purpose.

In addition to the nonlinearities of the flux linkage characteristics, the LVRM could suffer from the hysteresis problem. Basically, the hysteresis effect becomes more significant when the airgap width between the stator and the rotor decreases. An experiment is conducted to measure the hysteresis nonlinearity versus change of the airgap width. The results are shown in Fig. 7, where x axis is the phase winding A current and y axis the measured flux. When the airgap width is reduced to almost zero, the hysteresis band becomes very large and this hysteresis effect contributes additional nonlinearity on the motor model. However, when the airgap width increases, the hysteresis loop area decreases. For our designed example, the airgap width is set to be 0.4 mm. From Fig. 7, we find that the hysteresis band for the phase current is $\Delta A = \pm 0.4$ A (<5% of the maximum current) and the hysteresis band for the flux linkage is $\Delta\lambda = \pm 4.5$ mWb (<5% of the maximum flux level); therefore, the nonlinearity modeling due to the hysteresis effect is negligible for the proposed LVRM design.

In summary, the basic characteristics of the proposed actuator are investigated completely. The proposed LVRM is concluded to be a nonlinear device and there is no generic scheme for the driving of the proposed actuator. A novel driving scheme for the proposed LVRM that has high speed, high accuracy, and low force ripple needs to be developed [16].

IV. Control Strategy

Exploiting the fact that the current dynamics are at least an order faster than the mechanical dynamics, this paper proposes a dual-rate cascade control approach. A fast inner-loop current controller is employed to regulate the current–voltage nonlinearity of the actuator, while a slower outer-loop trajectory controller is used to control the mechanical dynamics. On top of this, a nonlinear function is included to compensate the nonlinearity of force against current and position. Fig. 8 is the overall block diagram of the control system.

A current controller is employed to linearize the current–voltage relation of the actuator. A proportional integral

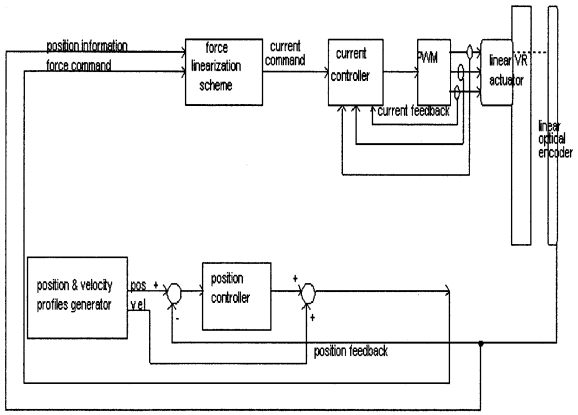

Fig. 8. Overall block diagram of the controller.

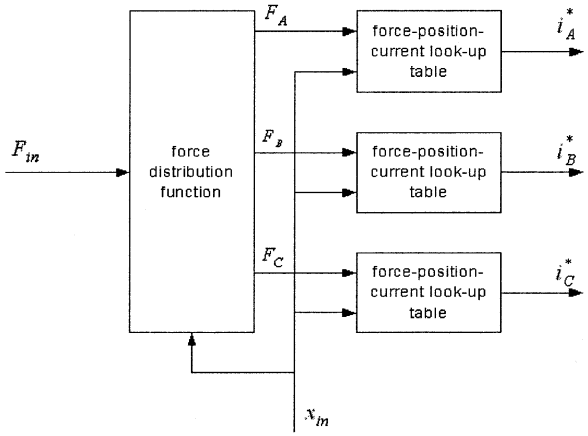

Fig. 9. Two-stage force-linearization scheme.

(PI) controller is proposed. The position can be assumed to be stationary during the control time frame of the current controller, since current dynamics are much faster than mechanical dynamics. The nonlinear function bridges the link between the trajectory controller and the current controller. It receives force commands and position information, and outputs desired current set points to the current controller.

The trajectory controller forms the essential part of the slow subsystem. It is a typical proportional integral derivative (PID) controller. Since the relations of force, current, and position are nonlinear in nature, a 3-D lookup table is employed in the force-linearization scheme.

The force-linearization scheme consists of two parts. The first part is to resolve the force command, $F_{\rm in}$, into three components, F_A, F_B, and F_C, and then for each phase, a current-force-position lookup table is employed to calculate the three-phase desired current i_A^*, i_B^*, and i_C^*. Fig. 9 shows the detailed block diagram of the force-linearization scheme.

Table II shows the phase-excitation table of the proposed linear actuator. For example, if the current position falls into region 5 and the required force command is a negative value, then phase B and/or phase C can be energized to produce the required force command; however, if the force command is a positive value, then only phase A can be energized to generate the command force. A linear function is proposed to perform the force distribution when two phase excitation is possible. Fig. 10

TABLE II
PHASE-EXCITATION TABLE FOR SINGLE-POLE PITCH

Region	Position range (mm)	+ve force command	-ve force command
1	0-1.6666	B	C,A
2	1.6666-3.3333	B,C	A
3	3.3333-5	C	A,B
4	5-6.6666	C,A	B
5	6.6666-8.3333	A	B,C
6	8.3333-10	B,A	C

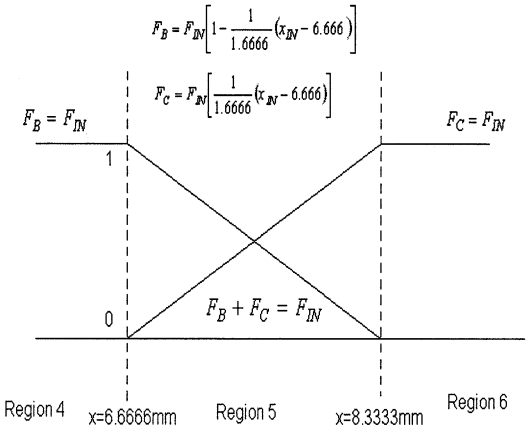

Fig. 10. Force-distribution function in region 5 for a negative force command.

shows a force-distribution example when the current position falls into region 5 and the force command is a negative value. Tables III and IV show the detailed force-distribution functions for both positive and negative force command. The proposed linear force-distribution function can improve the force transition between phase switching without any complex mathematical function implementation.

The current-force-position lookup table is the main component of the real-time controller, and is used to perform the force linearization. In Section III, we have developed the experimental current-force-position 3-D table; however, the data size ($61 \times 61 = 3721$ data points) may be too large for embedded low-cost microcontrollers/digital signal processors (DSPs). In the real-time controller implementation, we limit the table size within 512 data points so that the developed force-linearization scheme can be implemented using low-cost microcontrollers/DSPs with small memory spaces. The real-time controller stores sampled version of Fig. 6 and the table size is $21 \times 21 = 441$ data points. It is selected to fulfill the 512 data point requirement. Therefore, a 3-D lookup table using the 21×21 data matrix that is sampled from the original mesh, is developed for the real-time implementation of the motor controller. The 21×21 current-force-position 3-D chart is shown in Fig. 11.

Two-dimensional linear interpolation is used to find the intermediate values. Fig. 12 shows the method of obtaining the required current i^* by bi-linear interpolation. First, from the position $x_{\rm in}$ and force $F_{\rm in}$ inputs, two pairs of data in the lookup table $i_{(F_1,x_1)}$, $i_{(F_2,x_1)}$ and $i_{(F_1,x_2)}$, $i_{(F_2,x_2)}$ are located. For each pair, a linear interpolation is done, according to the ratio of F_1, F_2, and $F_{\rm in}$. As a result, two intermediate elements $i_{(F_{1-2},x_1)}$

TABLE III
FORCE-DISTRIBUTION TABLE FOR +VE FORCE COMMAND $F_{\rm in}$ ($x_{\rm in}$ IN MM)

Region	F_A	F_B	F_C
1	0	F_{in}	0
2	0	$F_{in}\left[1-\frac{1}{1.6666}(x_{in}-1.6666)\right]$	$F_{in}\left[\frac{1}{1.6666}(x_{in}-1.6666)\right]$
3	0	0	F_{in}
4	$F_{in}\left[\frac{1}{1.6666}(x_{in}-5)\right]$	0	$F_{in}\left[1-\frac{1}{1.6666}(x_{in}-5)\right]$
5	F_{in}	0	0
6	$F_{in}\left[1-\frac{1}{1.6666}(x_{in}-8.3333)\right]$	$F_{in}\left[\frac{1}{1.6666}(x_{in}-8.3333)\right]$	0

TABLE IV
FORCE-DISTRIBUTION TABLE FOR −VE FORCE COMMAND $F_{\rm in}$ ($x_{\rm in}$ IN MM)

Region	F_A	F_B	F_C
1	$F_{in}\left[\frac{1}{1.6666}x_{in}\right]$	0	$F_{in}\left[1-\frac{1}{1.6666}x_{in}\right]$
2	F_{in}	0	0
3	$F_{in}\left[1-\frac{1}{1.6666}(x_{in}-3.3333)\right]$	$F_{in}\left[\frac{1}{1.6666}(x_{in}-3.3333)\right]$	0
4	0	F_{in}	0
5	0	$F_{in}\left[1-\frac{1}{1.6666}(x_{in}-6.666)\right]$	$F_{in}\left[\frac{1}{1.6666}(x_{in}-6.6666)\right]$
6	0	0	F_{in}

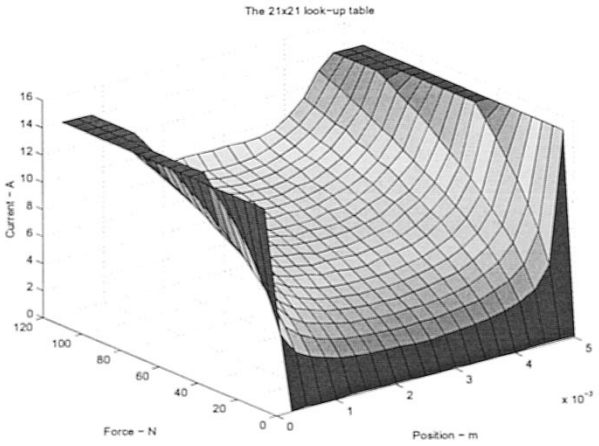

Fig. 11. The 21 × 21 current-force-position 3-D chart.

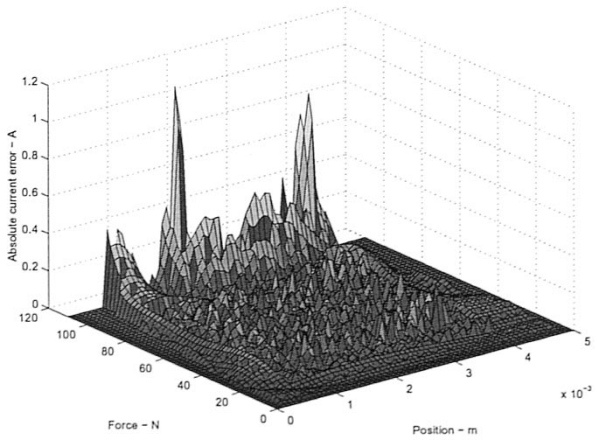

Fig. 13. Error analysis.

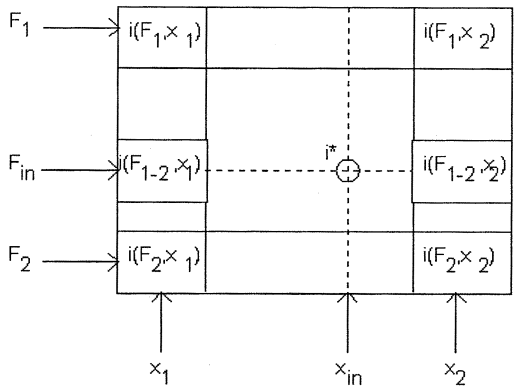

Fig. 12. Calculating i^* from the lookup table.

and $i_{(F_{1-2},x_2)}$ are obtained. Finally, the output current command i^* is obtained by interpolating the two intermediate elements with x_1, x_2, and $x_{\rm in}$.

To qualify the small but effective current-force-position lookup table, an error-budget analysis is performed. Fig. 13 shows the absolute error plot between the data interpolated by the proposed scheme and the actual experimental data. It is found that the maximum error is around 1 A, 10% of the maximum nominal current of the motor driver. The maximum error is located at the turning corners of the saturation region because a linear interpolation scheme is not capable of mimicking sharp turning corners. Except for the two small regions, the small lookup table can interpolate accurate data for other areas. This justifies the tradeoff between the size of the lookup table and the interpolation accuracy.

To show the effectiveness and the novelty of the proposed force-linearization scheme using the 3-D lookup table, simulation experiments are performed to tack a 100-mm position profile. The $21\times21=441$ small lookup table introduced in this section is employed in the motion controller while nonlinear motor model is constructed using the experimental data base obtained in Section III. Fig. 14 shows the force command input and also the corresponding three-phase force commands that are generated by the proposed linear force-distribution algorithm. The three-phase current commands, as shown in Fig. 15, are then evaluated using the 3-D lookup table. With the proposed simple but effective motion controller, accurate position tracking can be achieved. The dynamic position error between the command position and the actual position is less

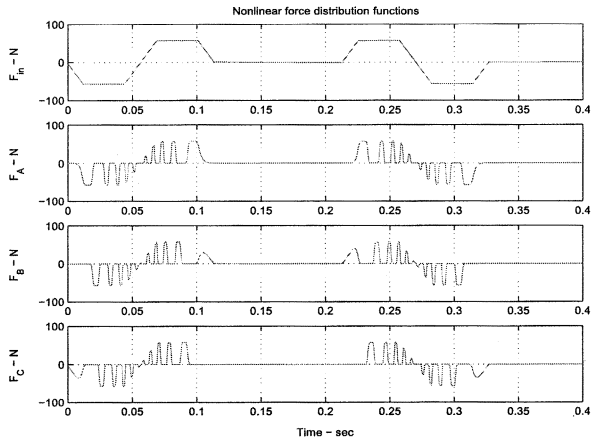

Fig. 14. Simulation results using the proposed nonlinear force compensation scheme (I).

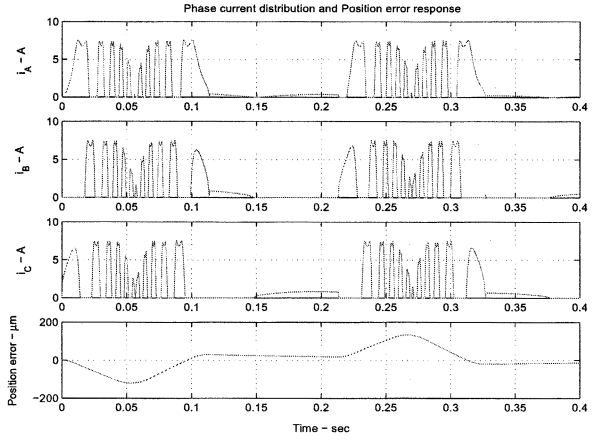

Fig. 15. Simulation results using the proposed nonlinear force compensation scheme (II).

than 200 μm and the static position error is less than 25 μm. The results are shown in the lower section of Fig. 15. In comparison to the conventional control algorithms proposed in [3], [8], our nonlinear control algorithm does not require the implementation of any complex mathematical functions such as sine, cosine and square root, etc. This novel feature is particularly suitable for the implementation of the proposed algorithm on low-cost fixed-point microcontrollers/DSPs.

V. Implementation

The controller is implemented on a DSP based system. Fig. 16 shows the schematic of the whole system while Fig. 17 shows the actual experimental setup at the power electronics laboratory in the Hong Kong Polytechnic University. A Pentium II computer is used for the program development and motion monitoring during the real time execution.

The mechanical resonance frequency of the proposed LVRM system with the dummy load attached, is found to be around 250 Hz by a swept-sine experiment. Hence, a position controller with a sampling frequency of 1 kHz was selected. This is more than adequate to accommodate the mechanical resonance of the LVRM. To ensure that the current loop is significantly faster than the position loop, a sampling frequency of 4 kHz was used.

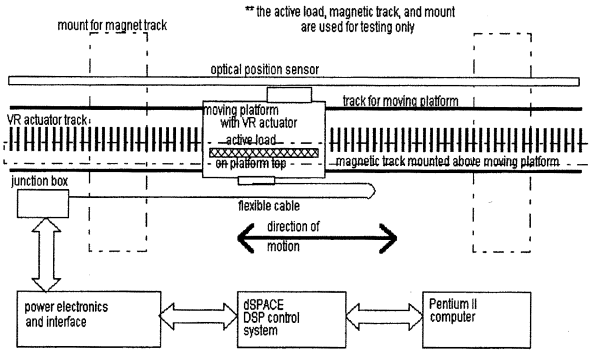

Fig. 16. Overall setup of the linear motion system.

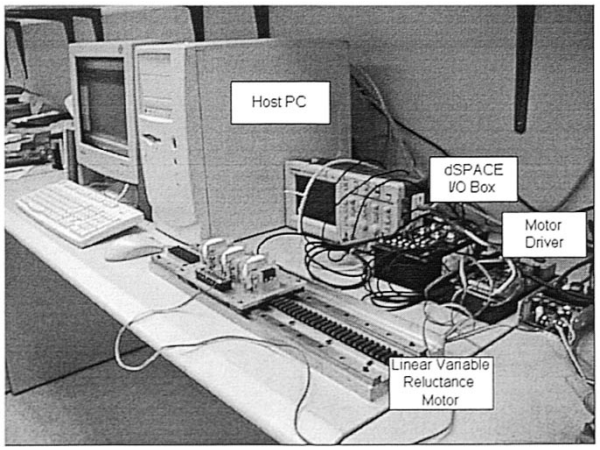

Fig. 17. Experimental setup at the power electronic laboratory in the Hong Kong Polytechnic University.

A DSP board, plugged into an Industry Standard Architecture (ISA) bus of a Pentium II computer, performs all control functions. The TMS320C31 DSP has a processing rate of 33 Mflops. Four simultaneous triggered analog-to-digital converters (two 16 bits, and two 14 bits) are included into the processor board. A TMS320P14 slave fixed-point DSP, which is tightly coupled to the TMS320C31, generates pulsewidth modulation waveforms. Notice that the present setup is intended for development purpose only. The proposed control scheme can be implemented on a low-cost DSP or even on a microcontroller.

For the power-electric drive of the LVRM, three asymmetric bridge insulated-gate bipolar transistor (IGBT) inverters are employed [1]. This structure facilitates a simple and effective current control loop so that high dynamic responses can be achieved in each motor phase. Since the pulsewidth modulation driver needs to have a chopping frequency that is substantially higher than the current-loop frequency, a chopping frequency of 12.5 kHz is selected. A voltage of 90 V is employed to supply the three asymmetric bridge IGBTs. The higher voltage ensures that the overall drive system has a better current dynamics.

A crossover protection circuit is used to protect the power supply from short-circuiting. Since the worst case turnoff time for the IGBTs are 0.5 μs, a 1-μs delay is introduced to the turn on of the IGBTs. The three-phase currents through the coils of the LVRM are sensed by three highly sensitive Hall effect elements. Three second-order analog active filters, with cutoff frequencies of 500 Hz are used to filter out the high-frequency components of current sensors.

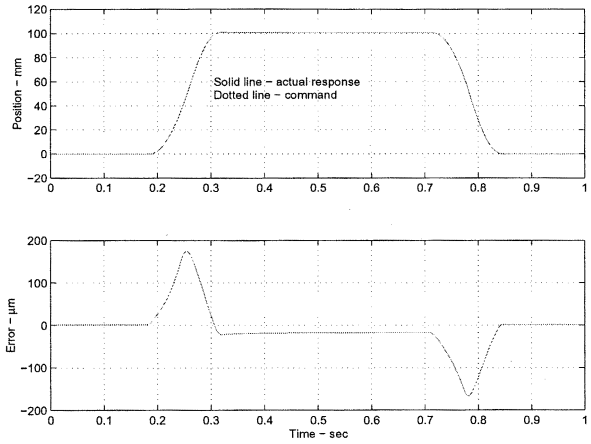

Fig. 18. Position response for the long-distance position profile.

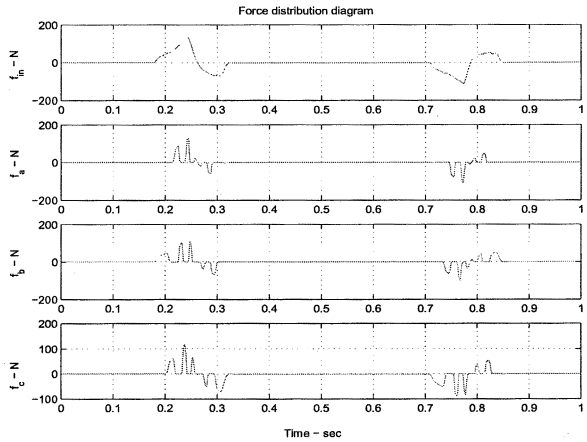

Fig. 19. Force-distribution diagram.

VI. Experimental Results

Two position profiles (100-mm and 250-μm traveling distances) are used as the test inputs. The first experiment is to test the tracking performance of the long-distance position profile. The full-load 5 kg is applied to the moving platform and the position response is shown in Fig. 18. The actual position tracks closely with the command position. The maximum dynamic error is approximately equal to 180 μm and the steady error is just below 20 μm which satisfies our design specifications.

The force command and the three-phase force distribution for the long-distance profile are depicted in Fig. 19. The maximum required force is about 120 N. The summation of the three-phase forces are equal to the command force. The result in Fig. 19 shows that the proposed force-distribution scheme and the lookup table force-linearization scheme work effectively without the implementation of complex mathematical functions such as sine, cosine and square root. Fig. 20 shows the actual current for the phase A motor winding. The maximum current requires to achieve the peak acceleration/deceleration is approximately equal to 11 A. This rating still falls into the motor amplifier driving capability. Hence, the long-distance position profile can still be tracked accurately.

The short-position profile needs to be investigated closely because small distance movements are indeed involved in many industrial applications such as pick-and-place movements and

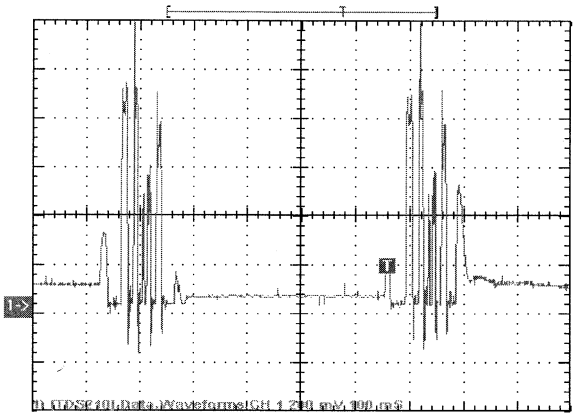

Fig. 20. Phase-A output current (100 mV = 1 A).

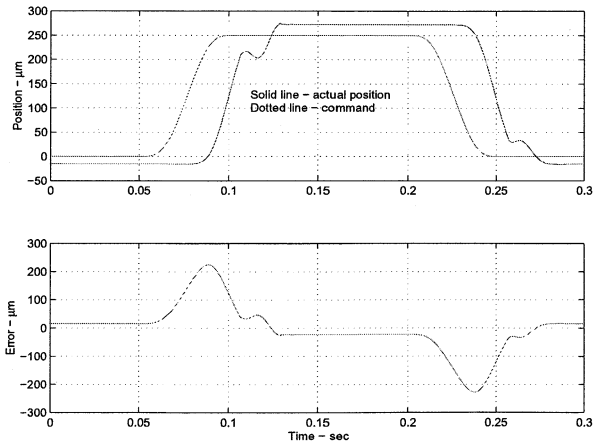

Fig. 21. Position response for the short-distance position profile.

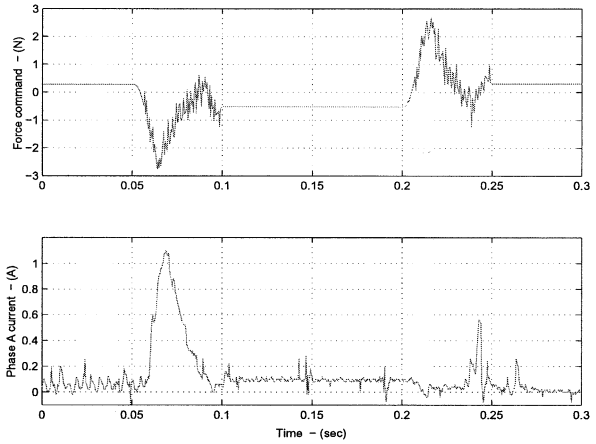

Fig. 22. Total force command and the phase-A current for the short-distance position profile.

the semiconductor bonding processes. Fig. 21 shows the position response when the 250-μm short-distance position profile is used as the test input. Although overshoot and nonlinear effects are present at the output, the steady state error is just below 25 μm, which still satisfies the design specifications. Fig. 22 shows the internal dynamics of the position control system in response to this short position profile. The upper section shows the total force command while the lower section depicts the corresponding phase current for winding A.

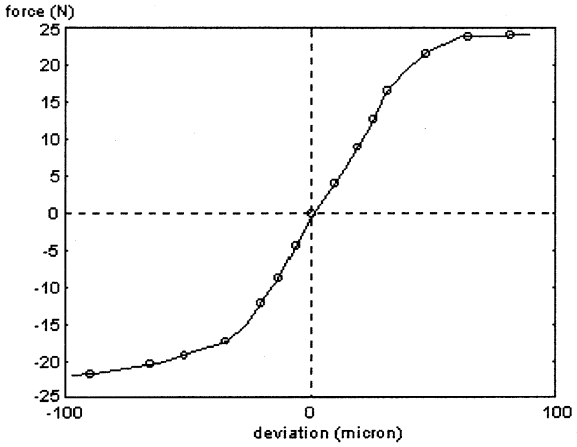

Fig. 23. Stiffness of the control system around a set-point of 150 mm.

In addition to the position tracking responses, we also measured the static stiffness of the motion control system. The measured result that represents the stiffness of the control system is shown in Fig. 23. The restoring force acting on the motion platform is measured when it is deviated from its original set point position of 100 μm. The force-position profile is a familiar S-shape curve. There is a large force change around the $\pm$25-μm region, and then the force change becomes more gradual outside this region. The reasonably high stiffness of the system indicates that the system can be controlled to a high degree of accuracy. In summary, the proposed motion control system can follow the command path quite closely with a high stiffness.

VII. Conclusion

The variable-reluctance linear motion system described in this paper is robust, reliable and has little mechanical adjustments. Owing to its performance and low manufacturing cost, the actuator can be applied to many new and high-end applications which require high-precision and high-speed motions. It will also have a tendency to replace many traditional *X–Y* tables that operate by rotary motors and mechanical lead screws.

The variable-reluctance linear drive system uses a simple machine structure but a sophisticated control method. In this paper, an effective control method based on a cascade structure, a nonlinear lookup table, and dual-rate sampling is proposed and implemented. The proposed nonlinear control algorithm does not require any implementation of complex mathematical functions and is particularly suitable to be embedded in low-cost fixed-point microcontrollers/DSPs. Experimental results show that the linear variable-reluctance actuator can be operated at high acceleration/deceleration rate with high precision.

References

[1] T. J. E. Miller, *Switched Reluctance Motor and Their Control*. New York: Oxford Univ. Press, 1993.

[2] P. C. Kjaer, J. J. Gribble, and T. J. E. Miller, "High-grade control of switched reluctance machines," *IEEE Trans. Ind. Electron.*, vol. 33, pp. 1585–1593, Nov. 1997.

[3] D. M. Dawson, J. Hu, and T. C. Burg, *Nonlinear Control of Electric Machinery*. New York: Marcel Dekker, 1998.

[4] I. Boldea and S. A. Nasar, *Linear Electric Actuators and Generators*. Cambridge, U.K.: Cambridge Univ. Press, 1997.

[5] C. T. Liu and J. L. Kuo, "Experimental investigation and 3-D modeling of linear variable-reluctance machine with magnetic-flux decoupled windings," *IEEE Trans. Magn.*, vol. 30, pp. 4737–4739, Nov. 1994.

[6] W. C. Gan and N. C. Cheung, "Design of a linear switched reluctance motor for high precision applications," in *Proc. 3rd IEEE Int. Electric Machines and Drives Conf.*, June 2001, pp. 701–704.

[7] C. T. Liu, L. F. Chen, J. L. Kuo, Y. N. Chen, Y. J. Lee, and C. T. Leu, "Microcomputer control implementation of transverse flux linear switched reluctance machine with rule-based compensator," *IEEE Trans. Energy Conversion*, vol. 11, pp. 70–75, Mar. 1996.

[8] H. K. Bae, B. S. Lee, P. Vijayraghavan, and R. Krishnan, "A linear switched reluctance motor: converter and control," *IEEE Trans. Ind. Appl.*, vol. 36, pp. 1351–1359, Sept. 2000.

[9] B. S. Lee, H. K. Bae, P. Vijayraghavan, and R. Krishnan, "Design of a linear switched reluctance machine," *IEEE Trans. Ind. Appl.*, vol. 36, pp. 1571–1580, Nov. 2000.

[10] J. Lucidarme, A. Amouri, and M. Poloujadoff, "Optimum design of longitudinal field variable-reluctance motors-application to a high performance actuator," *IEEE Trans. Energy Conversion*, vol. 8, pp. 357–361, Sept. 1993.

[11] U. S. Deshpande, J. J. Cathey, and E. Richter, "A high force density linear switched reluctance machine," in *Proc. IEEE Industry Applications Society Annual Meeting*, vol. 1, Oct. 1993, pp. 251–257.

[12] J. Corda and E. Skopljak, "Linear switched reluctance actuator," in *Proc. 6th Int. Conf. Electrical Machines and Drives*, Sept. 1993, pp. 535–539.

[13] G. S. Buja and M. I. Valla, "Control characteristics of a SRM motor drives—Part II, operation in the saturated region," *IEEE Trans. Ind. Electron.*, vol. 41, pp. 316–325, June 1994.

[14] S. Bolognani, G. S. Buja, and M. I. Valla, "Switched reluctance motor performance analysis based on an improved model of its magnetic characteristics," *Elect. Mach. Power Syst.*, vol. 19, no. 4, pp. 425–438, 1991.

[15] M. F. Rahman, N. C. Cheung, and K. W. Lim, "Modeling of a nonlinear solenoid toward the development of a proportional actuator," in *Proc. 5th Int. Conf. Modeling and Simulation of Electrical Machines Convertors and Systems*, vol. 2, Sept. 1996, pp. 670–695.

[16] ——, "Converting a switching solenoid to a proportional actuator," *Trans. Inst. Elect. Eng. Jpn. D*, vol. I-16, no. 5, pp. 531–537, 1996.

Wai-Chuen Gan (S'94–M'02) received the B.Eng degree (with first-class honors and the academic achievement award) in electronic engineering and the M.Phil. and Ph.D. degrees in electrical and electronic engineering from from The Hong Kong University of Science and Technology, Hong Kong, China, in 1995, 1997, and 2001, respectively.

From 1997 to 1999, he was a Motion Control Application Engineer at ASM Assembly Automation Ltd, Hong Kong, China He rejoined the same company in 2002 ,and is responsible for the development of the digital motor drivers. His current research interests include robust control of ac machines, power electronics, design and control of linear-switched reluctance motors, and control of stepping motors via interconnection and damping assignment.

Norbert C. Cheung obtained the B.Sc.degree from from the University of London, London, U.K., the M.Sc.degree from the University of Hong Kong, Hong Kong, China, and the Ph.D. degree from the University of New South Wales, Sydney, Australia, in 1981, 1987, and 1995, respectively.

From 1981 to 1985, he was an Electronic Engineer in industry, in the areas of servo drives and industrial electronics. During this period, he was the Project Leader for the development of Hong Kong's first Photoplotter System; a high precision CNC light-plotting machine for PCB production. From 1985 to 1992, he was a Lecturer/Senior Lecturer in the Department of Electrical Engineering, Hong Kong Polytechnic, Hong Kong, China, where he is curenlty a Lecturer. Before he rejoined the Hong Kong Polytechnic University, he worked for two years at ASM Assembly Automation, Hong Kong, China, in the areas of intelligent motion control and robotic systems for semiconductor manufacturing. His research interests are motion control systems, actuators design, and motor drives.